Nanoscale

PAPER

View Article Online
View Journal | View Issue

Cite this: *Nanoscale*, 2019, **11**, 20245

Published on 08 October 2019. Downloaded by ASU Library on 9/3/2020 5:05:54 AM.

Anomalous phase transition behavior in hydrothermal grown layered tellurene†

Han Li,[a] Kedi Wu,[a] Sijie Yang,[a] Tara Boland,[a] Bin Chen,[a] Arunima K. Singh[b] and Sefaattin Tongay *[a]

Received 2nd August 2019,
Accepted 8th October 2019

DOI: 10.1039/c9nr06637c

rsc.li/nanoscale

Recent studies have demonstrated that tellurene is a van der Waals (vdW) two-dimensional material with potential optoelectronic and thermoelectric applications as a result of its pseudo-one-dimensional structure and properties. Here, we report on the pressure induced anomalous phase transition of tellurium nanoribbons. The observation of clean phase transitions was made possible with high quality single crystalline Te nanoribbons that are synthesized by hydrothermal reaction growth. The results show that phase transition has a large pressure hysteresis and multiple competing phases: during compression, the phase transition is sudden and takes place from trigonal to orthorhombic phase at 6.5 GPa. Orthorhombic phase remains stable up to higher pressures (15 GPa). In contrast, phase transition is not sudden during decompression, but orthorhombic and trigonal phases co-exist between 6.9 to 3.4 GPa. Grüneisen parameter calculations further confirm the presence of co-existing phases and suggest hysteretic phase change behavior. Finally, orthorhombic to trigonal phase transition occurs at 3.4 GPa which means overall pressure hysteresis is around 3.1 GPa.

Introduction

Tellurium has attracted increasing interest due to its unique pseudo-one-dimensional structure that gives rise to outstanding thermoelectric[1–5] and electronic[5–8] properties. In tellurene, tellurium atoms form helically arranged chains along the *c*-axis of the unit cell. These chains are relatively weakly coupled to each other through van der Waals (vdW) interactions which results in the formation of tellurene sheets stacked onto each other.[9] Because of its vdW layered as well as unique quasi-1D chain like nature, the physical properties of Te under high pressures could be very different compared to classical bulk or conventional layered materials systems. Especially after the successful synthesis of highly crystalline layered tellurene sheets, it is possible to study their unique properties under extreme pressures.

While the structural behavior of bulk Te has long been studied at high pressures,[10–14] these studies were performed on semi-amorphous powders which doesn't allow one to probe fundamental properties of these 2D tellurene. Currently, there is no information on high pressure behavior of 2D tellurene sheets mostly due to the difficulties in preparation of high-quality nanoscale samples as well as integration with high pressure diamond anvil cell (DAC) chamber. Lastly, there is a controversy in the current literature regarding to tellurium under high pressure: although it has been established that tellurium undergoes phase transition, the phase transition pressure and the identity of high-pressure phase have been under dispute.[10,11,13,15–18] X-ray diffraction used for high pressure studies is often limited by the amount of samples that can be loaded into the DAC chamber, leading to low signal-to-noise ratio in the spectra collected, and ambiguous interpretation.

With recent advances in the 2D materials field, both issues with sample synthesis and characterization of high-pressure phase are readily solved. Multiple techniques have been developed for preparation of tellurium nanoribbons/nanoplates/nanocrystals. In particular, facile hydrothermal synthesis routes have been established for Te nanoribbons with good control over sample dimensions and high crystallinity.[8,19] Meanwhile, Raman spectroscopy has emerged as a powerful tool for investigation of phase transition since Raman spectra from different phases are vastly different. One advantage of Raman spectroscopy over XRD is that the sensitivity of Raman spectroscopy is significantly higher when sample size is small, making it an ideal choice for studying pressure-induced phase transition of nanomaterials.

This work marks the first observation of phase transition hysteresis in pseudo-one-dimensional tellurene sheets. Our efforts focus on identification of phase transition in ultrathin

---

[a] *School for Engineering of Matter, Transport and Energy, Arizona State University, Tempe, Arizona 85287, USA. E-mail: sefaattin.tongay@asu.edu*

[b] *Department of Physics, Arizona State University, Tempe, AZ 85287, USA*

† Electronic supplementary information (ESI) available. See DOI: 10.1039/c9nr06637c

View Article Online

Published on 08 October 2019. Downloaded by ASU Library on 9/3/2020 5:05:54 AM.

Te nanoribbons under hydrostatic pressure by Raman spectroscopy. Pressure dependent Raman spectra recorded in a DAC system under different pressure have demonstrated a sudden change at 6.5 GPa where the characteristic peaks from trigonal phase Te disappear and two new peaks at 40 and 100 cm^{-1} emerge. However, when the applied pressure is released, reverse phase transition is observed at a lower pressure of 3.4 GPa. Our comprehensive Raman peak analysis along with density functional theory (DFT) simulations reveal that the high-pressure phase is orthorhombic while the anomalous crossover region is caused by co-existence between orthorhombic and monoclinic phases. Results are discussed together with comprehensive DFT studies to give further insights into the nature of such anomalous phase transition effects.

2D vdW tellurium growth

vdW Te nanoribbons were synthesized by hydrothermal reaction growth.[8,20,21] In a typical process, 100 mg sodium tellurite, 15 μL hydrazine, and 50 μL ammonia were mixed with DI water and in an autoclave. The autoclave is then sealed and heated at 160 °C for 20 hours. After cooling and removal of excess reagents and byproducts, the resulting Te nanoribbons are characterized by SEM, TEM, EDX, and Raman spectroscopy. SEM image shown in Fig. 1a demonstrates needle-like features with length varying between 0.1 and 100 μm. Our low magnification TEM image (Fig. 1b) also shows 1D structure of the Te nanoribbons, and the selected area electron diffraction (SAED) pattern ([−110] zone axis) recorded from these nanoribbons indicate that the lattice parameters are $d(001) = 0.589$ nm and $d(110) = 0.221$ nm respectively (Fig. 1b inset). EDS spectrum collected from the sample shows only Te signals other than background from substrate, confirming the elemental composition of the Te nanoribbons (Fig. 1c). Raman spectrum from these hydrothermal Te also confirms the trigonal phase and high crystallinity as the FWHM of Raman peaks are below 5 cm^{-1} (Fig. 1d). Furthermore, angle-resolved Raman spectroscopy (ARS) measurements on these Te nanoribbons show that all three Raman peaks demonstrate strong angle-dependent intensities, which are consistent with literature.[8,22] Overall results suggest that Te nanoribbon from hydrothermal reaction is indeed trigonal vdW phase Te with high crystallinity.

Phase transition under pressure

Next, we have studied the material behavior under hydrostatic pressure in DAC chamber. Te nanoribbon samples were dispersed in 4 : 1 mixture of methanol and ethanol as pressure media to introduce hydrostatic pressure. The dispersed sample was then loaded into the DAC gasket and aligned with the optical path of the Raman spectrometer. The pressure near Te vdW sheets were measured using fluorescence of ruby as a pressure gauge. The pressure in the gasket was gently increased and Raman spectra of Te were recorded at each pressure point. As shown in Fig. 2a, phase transition of Te nanoribbon was observed at 6.5 GPa during compression as

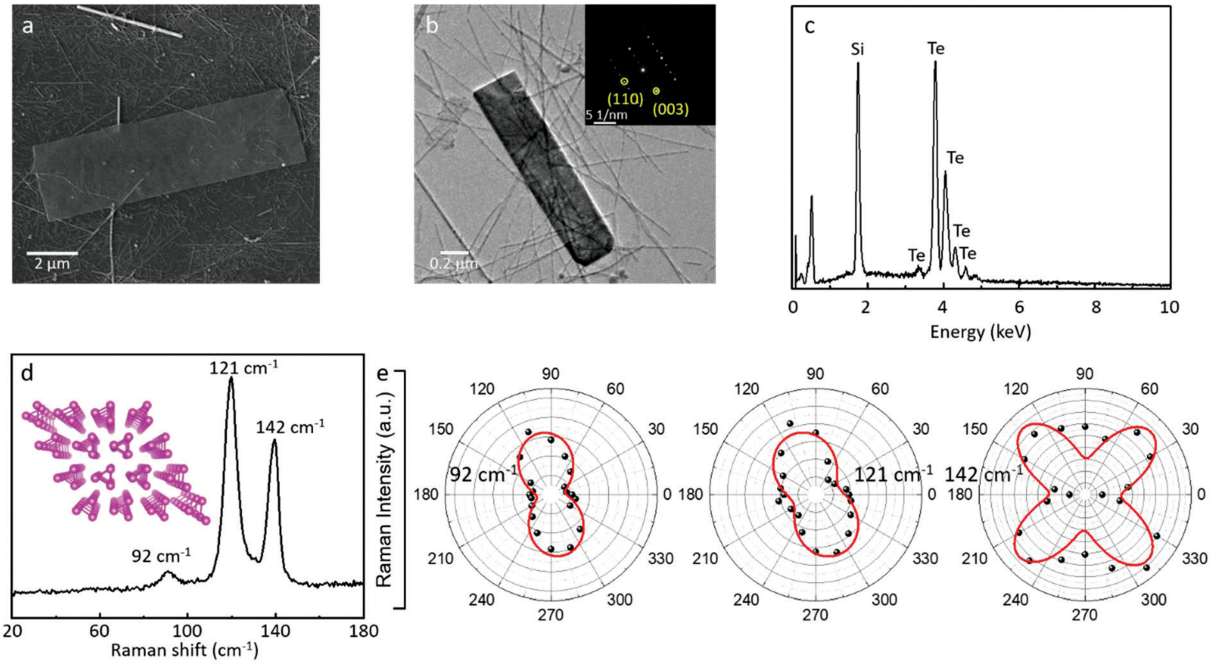

Fig. 1 Characterization of hydrothermal Te nanoribbons a. SEM image of hydrothermal Te nanoribbons. b. Low magnification TEM image of Te nanoribbons. Inset: SAED pattern of Te nanoribbons. c. EDS spectrum of Te nanoribbons. d. Raman spectrum of Te nanoribbons. Inset: Structural model of trigonal phase Te. e. Polar plots of 92, 121, and 142 cm^{-1} peak intensities of Te nanoribbons.

This journal is © The Royal Society of Chemistry 2019

View Article Online

Published on 08 October 2019. Downloaded by ASU Library on 9/3/2020 5:05:54 AM.

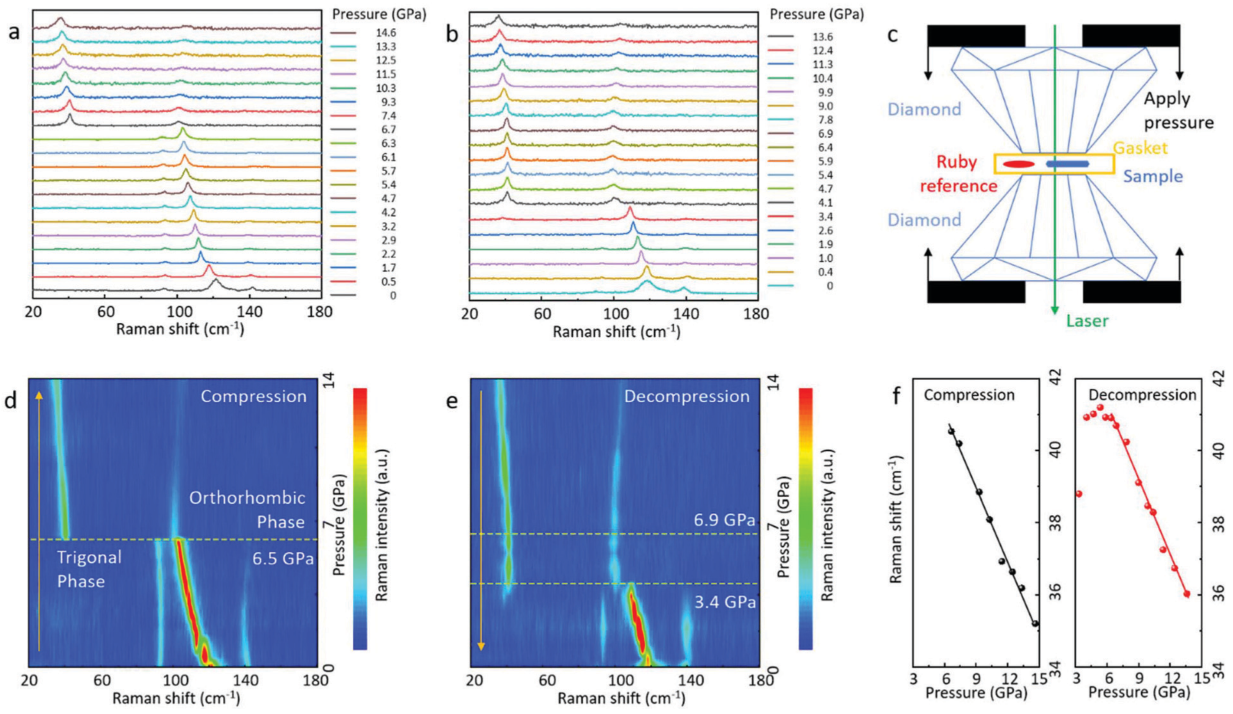

Fig. 2 Pressure induced phase transition of tellurium nanoribbons. a–b. Raman spectra of Te nanoribbon during a. compression and b. decompression. c. Schematics of diamond anvil cell. d–e. Contour plot of Te nanoribbon Raman intensity during d. compression, e. decompression. f. Pressure dependence of 40 cm^{-1} Raman peak position during compression (black) and decompression (red).

evidenced by a sudden change in Raman spectrum: the 92, 121, and 142 cm^{-1} peak of trigonal phase Te disappeared and two new peaks at 40 and 100 cm^{-1} emerged. The phase transition pressure of 6.5 GPa is consistent with previously reported results, and the 100 cm^{-1} Raman peak after phase transition is in good agreement with the theoretical predictions and experimental observations for the characteristic Raman peak of orthorhombic Te at high pressure.[18] We find that further increasing pressure up to 14 GPa does not yield any changes in the Raman spectra, implicating that there is no additional phase transition in this pressure range.

Upon reaching 14 GPa, the pressure in the DAC gasket was slowly released and Raman spectra of Te were recorded again at each pressure point. The results presented in Fig. 2b suggest that a reverse phase transition from high-pressure phase to trigonal phase has occurred in this process as evidenced by distinct Raman peaks from both phases.

However, careful examination of these Raman spectra reveals that phase transition during decompression exhibited hysteresis-like features: the phase transition point during pressure decompression was observed at 3.4 GPa, which is significantly lower compared to phase transition pressure during compression at 6.5 GPa (Fig. 2d and e). Additionally, the Raman spectrum underwent a sharp change from trigonal phase to high-pressure phase during compression, but during decompression, the transition was not as sharp. Notably, we observed characteristic peaks from trigonal phase as well as one peak at 40 cm^{-1} in one Raman spectrum recorded at 3.4 GPa, suggesting co-existence of both phases. Moreover, the 40 cm^{-1} Raman peak exhibited slightly different pressure dependence in compression/decompression processes (Fig. 2f): during compression, 40 cm^{-1} peak redshifts as the pressure increases and the peak position changes linearly with pressure between 6.5 and 15 GPa. The same peak exhibits a linear blueshift with decreasing pressure, but only between 15 and 6.9 GPa. Below 6.9 GPa, the 40 cm^{-1} peak shows minimal shift as the pressure decreases until phase transition to trigonal phase occurs at 3.4 GPa.

To summarize, the phase transition of Te nanoribbons exhibit hysteretic behavior as evidenced by: 1. a significantly lower phase transition pressure between trigonal and high-pressure phase; 2. observation of co-existing phases; 3. unusual pressure dependence of 40 cm^{-1} Raman mode during decompression. We speculate that the origin of such unusual phase transition is competition between multiple phases near 6.5 GPa. As multiple Te phases have been reported near 6.5 GPa, it is possible that they have similar formation energy at that pressure and co-existing phases can form. Determining the identities of each phase before/after phase transition will be critical for revealing the nature of hysteretic phase change behavior.

We focused our theoretical efforts on determination of Te phases above 6.5 GPa, as well as between 6.9 and 3.4 GPa. Six Te structures (Table S1†) are selected as possible candidates and their normal mode phonon frequencies at different pressure points are calculated by density-functional theory

Published on 08 October 2019. Downloaded by ASU Library on 9/3/2020 5:05:54 AM.

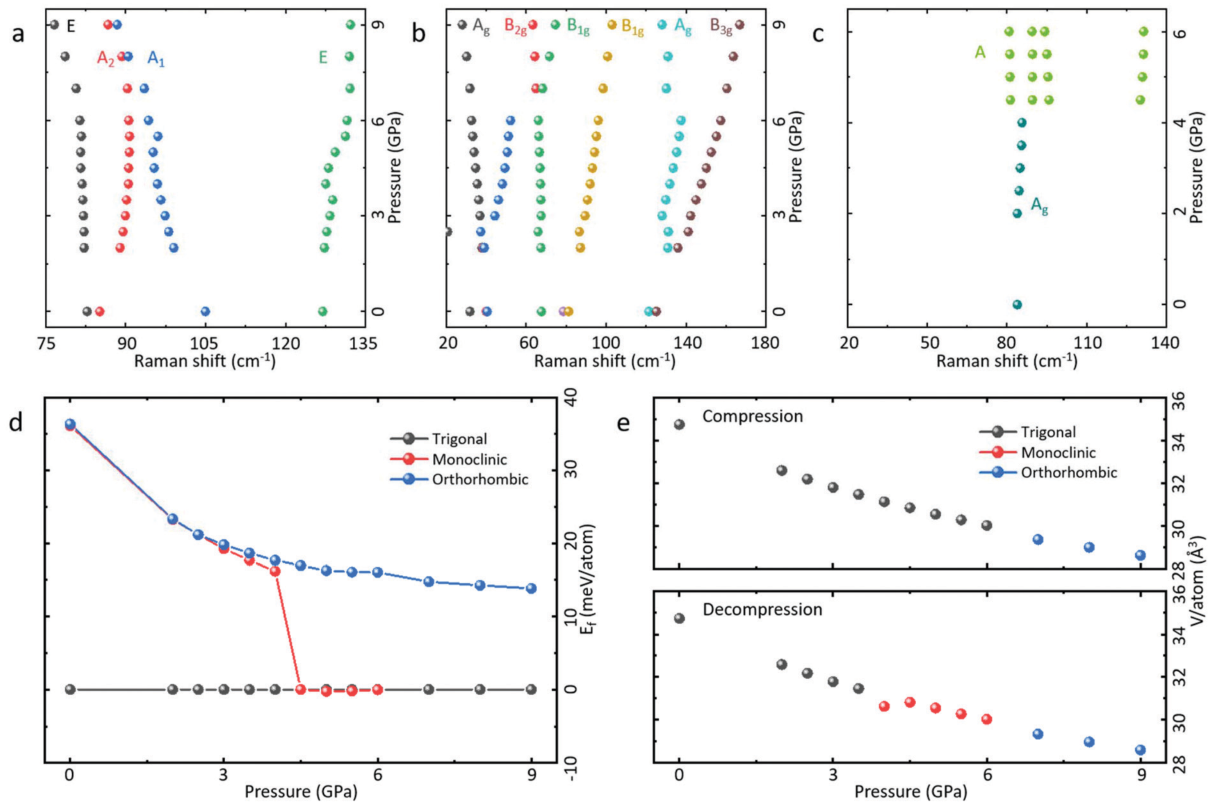

Fig. 3 DFT simulations of different Te phases under pressure. a–c. Simulated Raman modes of a. trigonal, b. orthorhombic, and c. monoclinic phases. d. Pressure dependence of formation energy from different Te phases between 0 and 9 GPa. e. Pressure dependence of the volume from different Te phases during compression and decompression.

(DFT) simulations (Fig. 3a–c, see S1† for full results). The normal mode phonon frequences include both Raman and IR active modes. To compare with theoretical predictions, Raman spectra collected in DAC experiments are carefully analyzed by plotting their peak position and FWHM against pressure during both compression and decompression (Fig. 4) For the low pressure phase, we find that the simulated A_2, A_1, and E modes from trigonal phase correlate well to 92, 121, and 142 cm^{-1} peaks, and the pressure dependencies of predicted modes also agree with our experimental observations (Fig. 3a and 4a). These agreements are further proof that the low-pressure phase is the trigonal phase. Likewise, the simulated results of the orthorhombic A_g mode and B_{1g} mode fit well with the 40 and 100 cm^{-1} Raman peaks in terms of both peak position and pressure dependence (Fig. 3b and 4b), which confirms the presence of the high-pressure, orthorhombic phase above 6.5 GPa. However, DFT simulations also suggest that there should be additional Raman modes for the orthorhombic phase above 6.5 GPa, which were not observed on our experiments. One possible explanation for this inconsistency is that the Raman peak intensity is extremely low during DAC experiments, therefore some of these peaks could have been undetected due to the low signal-to-noise ratio.

Focusing on the pressure region between 3.4 and 6.9 GPa during decompression where the abnormal Raman peak pressure dependence was observed. Raman spectra collected within this pressure range still resembles orthorhombic phase, but the pressure dependence of peak positions is significantly different.

The simulated pressure dependence of the volumes from the different Te phases for compression and decompression (Fig. 3e) are provided and the Grüneisen parameter for each pressure region is calculated to better demonstrate the small difference between pressure regions. Above 6.9 GPa, the Grüneisen parameter calculated for the 40 cm^{-1} peak is −1.35 during compression and −1.43 during decompression. The small difference of 5.9% between the two figures suggest that their corresponding phases are the same orthorhombic phase. In the 3.4–6.9 GPa pressure range, the Grüneisen parameter for the 40 cm^{-1} peak is only −0.02, significantly larger compared to that of the higher-pressure range. We speculate that this is caused by the formation of a metastable monoclinic phase that co-exists with the orthorhombic phase in this pressure range. DFT simulations suggest that this phase is unstable below 4 GPa as evidenced by a negative phonon frequencies (Fig. S1e†). DFT simulations also suggest that the monoclinic phase above 6.5 GPa can't retain its monoclinic structure, suggesting that it is only stable between 4 and 6.5 GPa. Simulated Raman modes of monoclinic phase (Fig. 3c) consist of multiple A modes, one of which is located ~95 cm^{-1}

Published on 08 October 2019. Downloaded by ASU Library on 9/3/2020 5:05:54 AM.

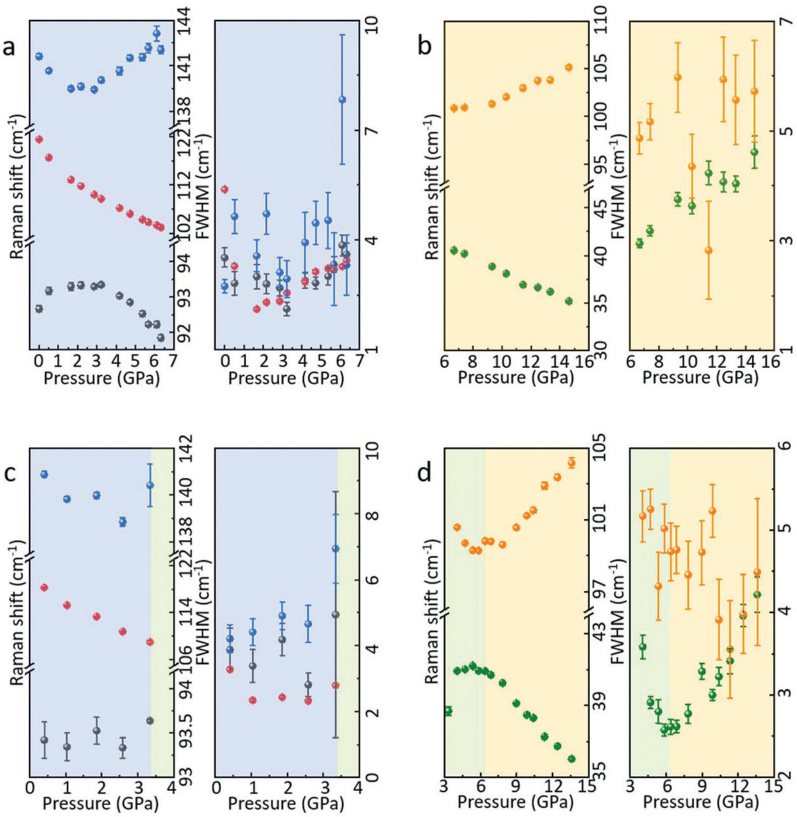

Fig. 4 Raman peak analysis during pressure induced phase transition. a–b. Raman peak position and FWHM of a. trigonal phase and b. high-pressure phase during compression. c–d. Raman peak position and FWHM of c. trigonal phase and d. high-pressure phase during decompression. Different phase regions are indicated by transparent background: blue: trigonal; yellow: orthorhombic; green: monoclinic + orthorhombic.

and has a small pressure dependence similar to experimental results. However, no Raman mode close to 40 cm^{-1} is predicted for the monoclinic phase, which provides further evidence that the intermediate phase can't be the monoclinic phase alone. For this reason, we speculate that the 40 cm^{-1} peak observed between 3.4 and 6.9 GPa during decompression originates from the orthorhombic phase, and its abnormal pressure dependence is caused by co-existence of monoclinic and orthorhombic phases.

To investigate the phase stability of the phase transitions observed in Te, we calculated the formation energy (E_f) between 0 to 9 GPa of the three phases we experimentally observed. E_f of the trigonal phase is set as a zero reference in the calculation and the results are presented in Fig. 3d. At low pressure (<3 GPa), both orthorhombic and monoclinic phases have positive formation energy, suggesting trigonal phase should be the stable phase in this pressure range. Near 4 GPa, the E_f of the monoclinic phase suddenly decreases and becomes similar to the E_f of the trigonal phase, which matches with the phase transition pressure from monoclinic to trigonal phase during decompression. As for the orthorhombic phase, its E_f decreases with increasing pressure, although it remains positive even at 9 GPa. However, we note that the E_f above 6 GPa is below 15 meV per atom, which is smaller than thermal energy at room temperature ($k_bT \sim 25$ meV), suggesting that the orthorhombic phase could be the stable phase in this pressure regime. Overall, the simulated E_f trend of different phases are consistent with the observed phase transition pressures.

The fundamental origin of anomalous pressure hysteresis in vdW tellurene sheets is less straight-forward. One potential explanation is related to the energy activation barrier differences across three competing trigonal, monoclinic, and orthorhombic phases. During the compression, if the energy barrier between trigonal–orthorhombic phase transition is very close but less than that of trigonal–monoclinic transition, the material will naturally undergo trigonal–orthorhombic transition. For decompression, however, the material is stable in orthorhombic phase high-pressures and seeks to transform into other phases to lower its energy. In this particular phase, crystal structure, and local strain environment, our data suggests that the energy barrier is lower for orthorhombic–monoclinic phase compared to orthorhombic–trigonal transition. In other words, these results suggest that the energy barrier is not isotropic but direction (compression *vs.* decompression) dependent. Here, future work is needed in the community to address some of the open questions to better illustrate hysteresis mechanism and how competing phases co-exist.

Published on 08 October 2019. Downloaded by ASU Library on 9/3/2020 5:05:54 AM.

Conclusion

High pressure studies shows that vdW Te sheets display anomalous pressure behavior compared to other vdW layered material systems. The onset of trigonal to orthorhombic phase transition is quite different under compression (~6.5 GPa) and decompression (~3.4 GPa). During decompression process, there exist co-existing pressure range (6–3 GPa) where multiple phases compete with each other. DFT simulations together with Grüneisen parameter analysis suggest that the intermediate region between 3.4 and 6.9 GPa is a co-existing phase between orthorhombic and monoclinic phases. Results presented offer the first pressure studies on highly crystalline vdW tellurene sheets and extend our understanding of this unique layered material system.

Methods

Hydrothermal synthesis

All chemicals are purchased from Sigma Aldrich and used as received. In a typical process, 100 mg sodium tellurite, 16 μL hydrazine, and 50 μL ammonia are combined in 10 mL deionized water in an autoclave. The autoclave is then sealed and maintained at 160 °C for 20 hours. After cooling to room temperature, the reaction mixture is centrifuged to isolate the precipitate, which is then rinsed with deionized water several times to remove excess reagents and impurities. The collected Te nanoribbons are then dispersed in select solvents for characterization (Raman, SEM, TEM, EDS) and DAC experiments.

Microscopy characterization

Scanning electron microscopy (SEM) and energy-dispersive X-ray spectroscopy (EDS) measurements were performed with AMRAY 1910 Field Emission SEM with working distance of 11–14 mm and an acceleration voltage of 20 kV. Transmission electron microscopy (TEM) image and diffraction patterns were recorded with FEI Titan 80-300 TEM at 300 keV with a spherical aberration corrector. SAED patterns were collected with a 10 μm aperture and a camera length of 380 mm. Results were processed with DigitalMicrograph 3 software.

Diamond anvil cell measurements

Hydrostatic pressure up to 15 GPa was applied to sample with a diamond anvil cell (DAC). Te nanoribbons and powder were dispersed in 4 : 1 mixture of methanol and ethanol as pressure media to introduce hydrostatic pressure. The sample was then placed in the gasket hole with 0.25 mm diameter. The pressure in the gasket was manually regulated and calibrated with ruby fluorescence. Raman spectra were recorded on a home-made Raman spectrometer with a 532 nm excitation laser in the backscattering configuration with 2400 mm^{-1} grating. The spot size of focused laser was ~1 μm and laser power was 2.30 mW.

Density functional theory calculations

All simulations are based on density-functional theory (DFT) using the projector-augmented wave (PAW) method as implemented in the plane-wave code VASP.[23–26] All the simulations were performed using the vdW-DF-optB88 exchange–correlation functional, that provides an excellent description of the non-local van der Waals interactions in materials.[27–29] All other pertinent details, including simulation parameters and the detailed discussion of the DFT results can be found in the ESI.†

Conflicts of interest

There are no conflicts of interest declared.

Acknowledgements

We acknowledge the use of facilities within the Eyring Materials Center at Arizona State University supported in part by NNCI-ECCS-1542160. We acknowledge Yi Zhou and Michael Durso for contribution to material synthesis. S. T. acknowledges support from NSF CMMI 1933214 and DMR 1552220. T. B. is funded by start-up funds from Arizona State University and U.S. Department of Energy grant number DE-SC0004954. This research used computational resources provided by the Texas Advanced Computing Center under Contract TG-DMR150006. This work used the Extreme Science and Engineering Discovery Environment (XSEDE), which was supported by National Science Foundation grant number ACI-1053575. The authors acknowledge Research Computing at Arizona State University for providing HPC resources that have contributed to the research results reported within this paper. URL: http://www.researchcomputing.asu.edu.

References

1 S. Lin, W. Li, Z. Chen, J. Shen, B. Ge and Y. Pei, *Nat. Commun.*, 2016, **7**, 10287.
2 Z. Gao, G. Liu and J. Ren, *ACS Appl. Mater. Interfaces*, 2018, **10**(47), 40702–40709.
3 H. Peng, N. Kioussis and G. J. Snyder, *Phys. Rev. B: Condens. Matter Mater. Phys.*, 2014, **89**(19), 195206.
4 C. Dun, C. A. Hewitt, H. Huang, D. S. Montgomery, J. Xu and D. L. Carroll, *Phys. Chem. Chem. Phys.*, 2015, **17**(14), 8591–8595.
5 W. Wu, G. Qiu, Y. Wang, R. Wang and P. Ye, *Chem. Soc. Rev.*, 2018, **47**(19), 7203–7212.
6 T. Ikari, H. Berger and F. Levy, *Mater. Res. Bull.*, 1986, **21**(1), 99–105.
7 Z. Zhu, X. Cai, S. Yi, J. Chen, Y. Dai, C. Niu, Z. Guo, M. Xie, F. Liu, J.-H. Cho, Y. Jia and Z. Zhang, *Phys. Rev. Lett.*, 2017, **119**(10), 106101.

This journal is © The Royal Society of Chemistry 2019

Published on 08 October 2019. Downloaded by ASU Library on 9/3/2020 5:05:54 AM.

8 Y. Wang, G. Qiu, R. Wang, S. Huang, Q. Wang, Y. Liu, Y. Du, W. A. Goddard, M. J. Kim, X. Xu, P. D. Ye and W. Wu, *Nat. Electron.*, 2018, **1**(4), 228–236.
9 A. V. Hippel, *J. Chem. Phys.*, 1948, **16**(4), 372–380.
10 M. Takumi, T. Masamitsu and K. Nagata, *J. Phys.: Condens. Matter*, 2002, **14**(44), 10609–10613.
11 G. Parthasarathy and W. B. Holzapfel, *Phys. Rev. B: Condens. Matter Mater. Phys.*, 1988, **37**(14), 8499–8501.
12 Y. Akahama, N. Okawa, T. Sugimoto, H. Fujihisa, N. Hirao and Y. Ohishi, *Jpn. J. Appl. Phys.*, 2018, **57**(2), 025601.
13 J. C. Jamieson and D. B. McWhan, *J. Chem. Phys.*, 1965, **43**(4), 1149–1152.
14 A. Nishikawa, K. Niizeki and K. Shindo, *Jpn. J. Appl. Phys.*, 1993, **32**(S1), 48.
15 C. Hejny, S. Falconi, L. F. Lundegaard and M. I. McMahon, *Phys. Rev. B: Condens. Matter Mater. Phys.*, 2006, **74**(17), 174119.
16 K. Aoki, O. Shimomura and S. Minomura, *J. Phys. Soc. Jpn.*, 1980, **48**(2), 551–556.
17 P. W. Bridgman, *Phys. Rev.*, 1935, **48**(11), 893–906.
18 C. Marini, D. Chermisi, M. Lavagnini, D. Di Castro, C. Petrillo, L. Degiorgi, S. Scandolo and P. Postorino, *Phys. Rev. B: Condens. Matter Mater. Phys.*, 2012, **86**(6), 064103.
19 B. Mayers and Y. Xia, *J. Mater. Chem.*, 2002, **12**(6), 1875–1881.
20 M. Mo, J. Zeng, X. Liu, W. Yu, S. Zhang and Y. Qian, *Adv. Mater.*, 2002, **14**(22), 1658–1662.
21 Y. Du, G. Qiu, Y. Wang, M. Si, X. Xu, W. Wu and P. D. Ye, *Nano Lett.*, 2017, **17**(6), 3965–3973.
22 S. Yang, B. Chen, Y. Qin, Y. Zhou, L. Liu, M. Durso, H. Zhuang, Y. Shen and S. Tongay, *Phys. Rev. Mater.*, 2018, **2**(10), 104002.
23 G. Kresse and J. Hafner, *Phys. Rev. B: Condens. Matter Mater. Phys.*, 1993, **47**(1), 558–561.
24 G. Kresse and J. Hafner, *Phys. Rev. B: Condens. Matter Mater. Phys.*, 1994, **49**(20), 14251–14269.
25 G. Kresse and J. Furthmüller, *Phys. Rev. B: Condens. Matter Mater. Phys.*, 1996, **54**(16), 11169–11186.
26 G. Kresse and J. Furthmüller, *Comput. Mater. Sci.*, 1996, **6**(1), 15–50.
27 J. Klimeš, D. R. Bowler and A. Michaelides, *Phys. Rev. B: Condens. Matter Mater. Phys.*, 2011, **83**(19), 195131.
28 M. Dion, H. Rydberg, E. Schröder, D. C. Langreth and B. I. Lundqvist, *Phys. Rev. Lett.*, 2004, **92**(24), 246401.
29 G. Román-Pérez and J. M. Soler, *Phys. Rev. Lett.*, 2009, **103**(9), 096102.